

See discussions, stats, and author profiles for this publication at: <https://www.researchgate.net/publication/5563022>

Molecular Dynamics Simulation of the Energetic Room-Temperature Ionic Liquid, 1-Hydroxyethyl-4-amino-1,2,4-triazolium Nitrate (HEATN)

ARTICLE in THE JOURNAL OF PHYSICAL CHEMISTRY B · APRIL 2008

Impact Factor: 3.3 · DOI: 10.1021/jp710653g · Source: PubMed

CITATIONS

47

READS

58

4 AUTHORS, INCLUDING:



Wei Jiang

Argonne National Laboratory

19 PUBLICATIONS 971 CITATIONS

SEE PROFILE



Yanting Wang

Chinese Academy of Sciences

53 PUBLICATIONS 2,160 CITATIONS

SEE PROFILE

Molecular Dynamics Simulation of the Energetic Room-Temperature Ionic Liquid, 1-Hydroxyethyl-4-amino-1,2,4-triazolium Nitrate (HEATN)

Wei Jiang,[†] Tianying Yan,[‡] Yanting Wang,[†] and Gregory A. Voth^{*,†}

Center for Biophysical Modeling and Simulation and Department of Chemistry, University of Utah, Salt Lake City, Utah 84112-0850, and Institute of New Energy Material Chemistry, Nankai University, Tianjin 300071, China

Received: November 6, 2007; In Final Form: December 23, 2007

Molecular dynamics (MD) simulations have been performed to investigate the structure and dynamics of an energetic ionic liquid, 1-hydroxyethyl-4-amino-1,2,4-triazolium nitrate (HEATN). The generalized amber force field (GAFF) was used, and an electronically polarizable model was further developed in the spirit of our previous work (Yan, T.; Burnham, C. J.; Del Popolo, M. G.; Voth, G. A. *J. Phys. Chem. B* **2004**, *108*, 11877). In the process of simulated annealing from a liquid state at 475 K down to a glassy state at 175 K, the MD simulations identify a glass-transition temperature region at around 250–275 K, in agreement with experiment. The self-intermediate scattering functions show vanishing boson peaks in the supercooled region, indicating that HEATN may be a fragile glass former. The coupling/decoupling of translational and reorientational ion motion is also discussed, and various other physical properties of the liquid state are intensively studied at 400 K. A complex hydrogen bond network was revealed with the calculation of partial radial distribution functions. When compared to the similarly sized 1-ethyl-4-methyl-1,4-imidazolium nitrate ionic liquid, EMIM⁺/NO₃[−], a hydrogen bond network directly resulting in the poorer packing efficiency of ions is observed, which is responsible for the lower melting/glass-transition point. The structural properties of the liquid/vacuum interface shows that there is vanishing layering at the interface, in accordance with the poor ion packing. The effects of electronic polarization on the self-diffusion, viscosity, and surface tension of HEATN are found to be significant, in agreement with an earlier study on EMIM⁺/NO₃[−] (Yan, T.; Burnham, C. J.; Del Popolo, M. G.; Voth, G. A. *J. Phys. Chem. B* **2004**, *108*, 11877).

I. Introduction

Air- and water-stable ionic liquids (ILs) are organic salts with low melting points. ILs are entirely composed of ions and are liquids at ambient or far below ambient temperatures, sometimes as low as −96 °C. In recent years, ILs have received much attention in many areas of chemistry, for example, because of their potential utility as a novel environmentally friendly alternative to traditional organic solvents due to their nonvolatile character.^{1–3} Other IL properties include negligible vapor pressure, high electrical conductivity, high and adjustable dielectric constants, often excellent thermal, chemical, and electrochemical stabilities, nonflammability, ease of handling, and high ionic concentration. As a result, ILs are valuable in catalysis, synthesis,^{4–6} electrodepositions,⁷ and battery electrolytes.^{8,9} Other developments include hybrid materials based on the ILs with polymers and nanocarbons.^{10–14} More recently, substantial heterogeneities in imidazolium-based ILs (dry or wet) due to the intrinsic polar/nonpolar phase separation were found both experimentally^{4,6,15,16} and computationally,^{17–22} indicating that the ILs may be regarded as a nanostructured material.

The pioneering work of Wilkes²³ and King²⁴ in the 1960s explored low-melting-point salts, resulting in high-electric-current batteries. A key breakthrough was the study of 1-ethyl-3-methylimidazolium (EMIM⁺) cation,²⁵ obtaining a 25 °C

melting point for EMIM⁺/AlCl₄[−]. The later work of the Wilkes group²⁶ on the effect of changing the anion on the IL melting/glass-transition point helped to establish the current prevailing IL design principle that the low melting point of the ILs arises from the asymmetric large size of the ions, which decreases the strong Coulombic interactions present in general inorganic salts by delocalizing the charge distribution within each ion and also lowers the ion packing efficiency. These two effects in the large and asymmetric ions usually influence each other as seen, for example, in the non-monotonic evolution of melting points of imidazolium-based ILs.²⁷ By systematically synthesizing cations and anions with numerous combinations of substitutions, one is able to produce a large number of ILs, around ~10⁸, and thus, the physicochemical properties of the ILs can be tuned. Presently, the search for new ILs has been directed, for example, toward low-melting/glass-transition points, low viscosity, high conductivity, and high diffusivity.

Recently, attention has been paid to developing new energetic ILs^{28–32} since ILs have essentially no toxic vapor in the liquid state and therefore operational costs and risks may be lowered compared to traditional energetic materials. Room-temperature ionic liquids as a solvent are typically comprised of combinations of organic cations, such as imidazolium, pyridinium, pyrrolidinium derivatives, and bulky and soft anions. They are therefore considered chemically and thermally stable. However, for the chemically unstable energetic ILs, a central design criterion is the high heat of formation. As a result, the cations are replaced by triazolium- or tetrazolium-based ones, whose

* Author to whom correspondence should be addressed. E-mail: voth@chem.utah.edu.

[†] University of Utah.

[‡] Nankai University.

heterocyclic rings contain three and four nitrogen atoms, respectively, rather than the two nitrogens found in imidazolium ILs. The anions, on the other hand, can be replaced by nitrate, perchlorate, dinitramide, or picrate to provide more nitrogen atoms and a higher oxygen balance for self-combustion. Aside from chemical instability concerns, the design of energetic ILs is focused on obtaining a low-melting/glass-transition point, viscosity, and surface tension, all at a reasonably high density. Typical values of the melting/glass-transition point, viscosity, density, and surface tension for ideal IL fuels are, respectively, $-40\text{ }^{\circ}\text{C}$, $\leq 1\text{ poise}$ at $0\text{ }^{\circ}\text{C}$, $\geq 1.4\text{ g/cm}^3$, and $\leq 100\text{ dyn/cm}$.

Computational studies on energetic ILs have been devoted to various perspectives. Boatz, Gordon, and co-workers^{33,34} have performed systematic ab initio quantum chemistry calculations to study the effect of different substitution at the triazolium or tetrazolium ring nitrogen atoms on the heat of formation and charge delocalization, as well as the optimized geometric structure. Gutowski et al.³⁵ also studied the formation and stability of triazolium based ionic liquids based on ab initio electronic structure calculations. Alavi and Thompson³⁶ performed molecular dynamics (MD) simulations to investigate the solid/liquid-transition properties for the energetic IL 1-*n*-butyl-4-amino-1,2,4-triazolium bromide [part⁺][Br[−]], and its melting point was determined. In Cadena and Maginn's work,³⁷ thermophysical and transport properties of several triazolium-based ionic liquids were reported.

In the present study, MD simulations based on both electronically nonpolarizable and polarizable models have been carried out to investigate a newly designed energetic IL, 1-hydroxyethyl-4-amino-1,2,4-triazolium nitrate (HEATN). The intent in this work is to not only provide simulation data but also to provide insight into the relationship between molecular structure, dynamics, and other useful physical properties for this class of IL.

The remainder of this paper is organized as follows. In section II, the atomistic models and simulation methodology are described. Section III reports the MD simulation results, and a discussion is given. Section IV then provides concluding remarks.

II. Models and Computational Details

A. Electronically Nonpolarizable and Polarizable Models.

Both simulations and experiment have found that the local environment around IL ions is highly anisotropic. For such systems, it is desirable to have an electronically polarizable model which can reflect the electron density distortions by modeling charge fluctuation or induced dipole degree of freedom.^{38,39} Recently, Yan et al.⁴⁰ have developed a polarizable model for ionic liquids that relies on induced dipoles propagated within an extended Lagrangian approach to treat the many-body polarizability, similar in spirit to the Car–Parrinello method.⁴¹ Despite the increased computational cost, the polarization caused by the induced dipoles has been shown to have a significant influence on both the ion packing and the dynamical properties of ionic liquids.⁴⁰ The polarizable model also yields MD results in closer agreement with certain experimental data.

The total potential energy surface of the polarizable model is expressed by

$$V_{\text{polar}} = V_{\text{bond}} + V_{\text{nonbond}} + V_{\text{ind}} \quad (1)$$

where the V_{bond} , V_{nonbond} , and V_{ind} are expressed, respectively, as

$$V_{\text{bond}} = \sum_{\text{bonds}} \frac{1}{2} k_b (r - r_0)^2 + \sum_{\text{angle}} \frac{1}{2} k_\theta (\theta - \theta_0)^2 + \sum_{\text{dihedrals}} V_n \cos(n\phi - \gamma) \quad (2)$$

$$V_{\text{nonbond}} = \sum_i \sum_{j>i} \left(\frac{a_{ij}}{r_{ij}^{12}} - \frac{b_{ij}}{r_{ij}^6} + \frac{q_i q_j}{r_{ij}} \right) \quad (3)$$

$$V_{\text{ind}} = - \sum_i \mu_i \cdot \mathbf{E}_i^0 - \sum_i \sum_{j>i} \mu_i \cdot \mathbf{T}_{ij} \cdot \mu_j + \sum_i \frac{\mu_i^2}{2\alpha_i^2} \quad (4)$$

The term $V_{\text{bond}} + V_{\text{nonbond}}$ in eq 1 comprises the standard nonpolarizable IL model.

In the above equations, the force field parameters for the nonpolarizable model are provided in the generalized amber force field (GAFF)^{42,43} and have been employed in prior simulation work³⁶ on [part⁺][Br[−]]. For unlike atoms, the Lennard-Jones parameters were obtained from the Lorentz–Berthelot (LB) combining rules. The partial charges of both cations and anions were obtained by fitting the ab initio electrostatic potentials (ESP) with the RESP fitting package.⁴⁴ The ab initio calculations were performed with Gaussian 03.⁴⁵ The ESP grids were generated by MP2/aug-cc-pvdz and fit to the MP2/aug-cc-pvdz-optimized structure. The RESP partial charges are valid for both nonpolarizable and polarizable force field models.⁴⁰ In V_{ind} , the first term represents charge–dipole interactions, the second term represents dipole–dipole interactions, and the last term is the energy required to induce the dipole. In eq 4, \mathbf{E}_i^0 is the electric field on atom i , generated by the partial charges of all other atoms, excluding those within the same ion of atom i . The dipole field tensor \mathbf{T}_{ij} is calculated from the electrostatic potential $\phi(|\mathbf{r}_i - \mathbf{r}_j|)$ at point j due to the charge at point i such that $\mathbf{T}_{ij} = \nabla_i \nabla_j \phi(|\mathbf{r}_i - \mathbf{r}_j|)$. The induced dipole moment is given by

$$\mu_i = \alpha_i [\mathbf{E}_i + \sum_{j=1, j \neq i}^N \mathbf{T}_{ij} \cdot \mu_j]$$

where α_i is the isotropic atomic polarizability of atom i . By fitting the anisotropic molecular polarizabilities of the ions in the spirit of Thole's modeling methodology,⁴⁶ the effective isotropic atomic polarizabilities were determined to be 1.059, 0.243, 0.770, and 0.970 Å³ for the C, H, O, and N atoms of the cation, respectively, and 1.901 and 1.079 Å³ for the N and O atoms of the anion, respectively, with a smearing factor of 1.092. The all-atom model of HEATN is shown in Figure 1, with the atomic partial charges included. The details of the force field parameters can be found in the Supporting Information.

B. Molecular Dynamics Computational Details. Melting points have been measured and reported for the recently synthesized 1-substituted 4-amino-1,2,4-triazolium-based ionic liquids.⁴⁷ Some of the reported data actually correspond to the glass-transition temperature because a glass can sometimes form much more readily than the crystal. For those nitrate salts having cations substituted by short side chains, such as methyl or ethyl, the poor ion packing efficiency causes the ILs to tend to form a glass as the ambient temperature is lowered, and therefore, it is difficult to observe the resulting crystal structure.

MD simulations have played a fundamental role in understanding the dynamical changes that supercooled liquids undergo when approaching the glass-transition temperature.^{48–51} Since the melting/glass-transition point plays a significant role in the

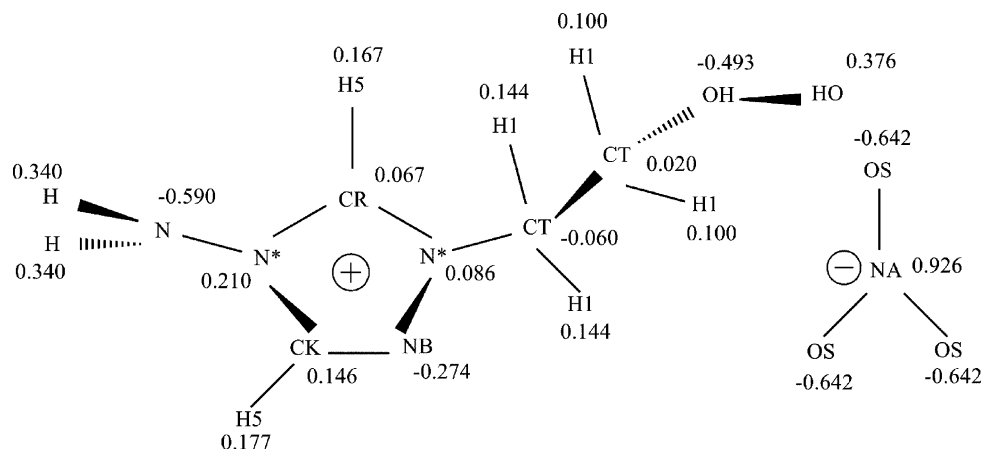


Figure 1. The molecular structure and the RESP fitted partial charges of the cation and anion.

design of ionic fuels, a key target of the present MD simulations was to estimate the glass transition via a simulated annealing method. In addition, useful liquid-state and liquid/vacuum interface properties relevant to ionic liquid fuels were studied with both the polarizable and nonpolarizable models at 400 K.

In the first set of studies, MD simulations to explore the glass-transition properties were performed with the nonpolarizable model. In the constant NPT ensemble, an initial configuration containing 216 ion pairs (4752 atoms) was manually constructed, with the ions positioned on the select lattice positions within a large cubic simulation box. The initial configuration was then pre-equilibrated at $T = 475$ K for 0.5 ns. The final configuration was then simulated for 0.5 ns in the constant NVT ensemble, and then, a 2.0 ns production run was performed. The temperature was then cooled to 150 K at intervals of 25 K. At each temperature, the same procedure of a 0.5 ns pre-equilibration followed by a 2.0 ns simulation was performed. The reason for choosing a constant NVT ensemble simulation instead of a constant NPT ensemble simulation is due to the limited size of the simulated systems, which causes fluctuations in the calculated volume that lead to inaccuracies in the determination of the glass transition from changes in the mean-squared molecular displacements.⁵⁰

In the second set of studies, a 216 ion pair initial configuration was equilibrated under constant NPT conditions at 400 K for 0.5 ns. The equilibrated densities were 1.436 g/cm³ for the polarizable model and 1.427 g/cm³ for the nonpolarizable model, which only differ by 0.63%. The final configuration was then used in a pre-equilibration run under constant NVT conditions for 0.5 ns, and finally a 5.0 ns production run was carried out. These procedures applied to both the polarizable and nonpolarizable models. For the production runs, the MD trajectory data were stored every 0.05 ps for the nonpolarizable model and 0.025 ps for the polarizable model.

In the third set of studies, a 128 ion pair initial configuration was equilibrated in the constant NPT ensemble at 400 K for 0.5 ns. The final configuration was then re-equilibrated under constant NVT conditions for 1.0 ns. This equilibrated 128 ion pair configuration was then duplicated once along the z direction to generate an initial configuration with 256 ion pairs. The new configuration was equilibrated at 1000 K in the constant NVT ensemble and then cooled down to 400 K at intervals of 200 K. At each different temperature, the system was equilibrated for 500 ps, adding up to a total pre-equilibration run of 2 ns. The pre-equilibrated configuration was then placed at the center of a larger supercell with an elongated z -cell length and the same x and y cell dimensions. The result was two equivalent

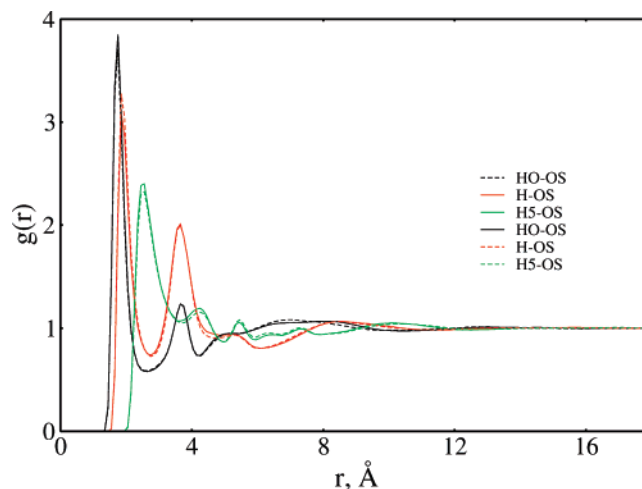


Figure 2. The partial radial distribution functions related to the hydrogen bond network. The solid lines denote the polarizable model, and dashed lines denote the nonpolarizable model.

ionic liquid–vacuum interfaces within a single supercell. MD simulations were then performed on these planar IL slabs in a constant NVT ensemble at 400 K. In all of the simulations, the supercell was set up using three-dimensional rectangular boundary conditions. The distance between two neighboring slabs was set to be 60 Å to eliminate the long-range interaction between them. The choice of the supercell sizes was aimed to keep a well-stabilized bulk-like region in the middle of the system, as well as to prevent the two equivalent interfaces from interacting with each other. The integration time step was 1.0 and 0.5 fs for the nonpolarizable and polarizable models, respectively. No detectable vaporization was observed during the simulations.

III. Results and Discussion

A. Structural Properties. The partial radial distribution functions (PRDFs) of the anion's oxygen (OS) and the cation's three types of polar hydrogen atoms, HO, H, and H5 (Figure 1), for both polarizable and nonpolarizable models, are shown in Figure 2. A distinct feature in Figure 2 is that strong spatial correlations can be observed. In addition to the strong H5–OS correlation that exists in imidazolium-based ILs,¹⁷ the HO–OS and H–OS groups form even more striking spatial correlations. Since the positions of these hydrogen atoms are highly distributed on the cations, it can be concluded that a complex hydrogen bond network forms in the bulk. Indeed, a snapshot randomly selected from the MD trajectory data is shown in Figure 3, where significant cation–anion contacts at atom HO,

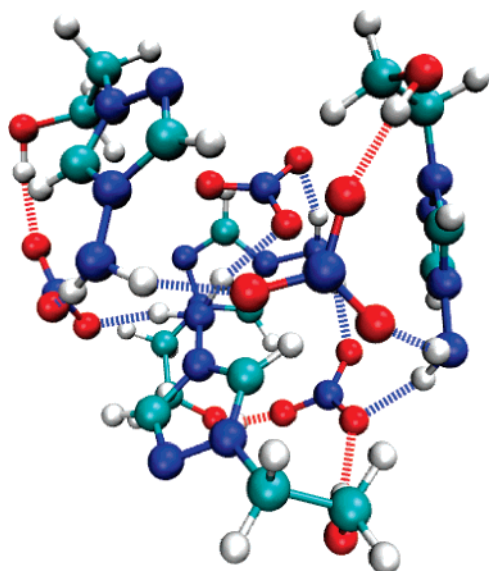


Figure 3. A snapshot randomly selected from the MD trajectory data, showing significant cation-anion contacts. The red dashed line and blue dashed line represent the HO-OS and H-OS hydrogen-bond interaction, respectively.

H, H5, and OS can be observed, with the red and blue dashed lines highlighting these significant hydrogen bonds.

The center-of-mass PRDFs of cation-cation $g_{++}(r)$, anion-anion $g_{--}(r)$, and cation-anion $g_{+-}(r)$, as well as those of EMIM⁺/NO₃⁻,⁴⁰ for both polarizable and nonpolarizable models, are shown in panels a, b, and c of Figure 4. A striking feature is the poorer packing efficiency of the cation and anion for HEATN. For example, two main peaks appear in $g_{+-}(r)$ due to the strong HO-OS and H-OS interactions. The heights (~ 1.5) of the main peaks are much smaller than that (~ 2.0) of EMIM⁺/NO₃⁻. It also can be seen that the long-range spatial correlation has been quenched in HEATN, relative to the nonvanishing long-range decay at ~ 18 Å for EMIM⁺/NO₃⁻.

To quantitatively investigate the characteristic length scale of the IL structural organization, the partial static structure factor, S_{ij} , corresponding to the PRDFs, g_{ij} , was calculated according to eq 5 below, where ρ is the number density of the centers-of-mass of interest and $S_{ij}(k)$ is given by

$$S_{ij}(k) = \delta_{ij} + \frac{4\pi\rho}{k} \int_0^\infty [g_{ij}(r) - 1] r \sin(kr) dr \quad (5)$$

The minimum k value was set to be $2\pi/L$, where the L is the side length of each simulation cell. The panels d, e, and f of Figure 4 show cation-cation, anion-anion, and cation-anion structure factors, respectively. The principal peaks of HEATN for $S_{++}(k)$ and $S_{--}(k)$ and the first minimum for $S_{+-}(k)$ are significantly less sharp than those of EMIM⁺/NO₃⁻, indicating that HEATN is less structured, as expected.

Figure 5 shows the three-dimensional isodensity plots for the preferred anion probability distribution around a central cation. It is seen that the distribution of anions forms a striking “helmet” structure. In contrast to the simpler anion probability distribution around the hydrogen atoms on the cation ring for imidazolium-based ILs,^{17,52} the complex packing pattern seen here for HEATN dramatically screens the long-range interactions between ions, thus implying a significantly lower melting/glass-transition temperature than that of imidazolium-based ILs.

B. Glass Transition. In the study of ionic liquids, the temperature dependence of the mean-squared displacements (MSD), the reorientation relaxation, structural relaxation, and

Van Hove self-correlation functions are important. For these properties, studies of other IL species have appeared previously in the literature.^{17,53}

Figure 6 shows the MSD, $\langle \Delta r(t)^2 \rangle$, for both the cation and anion at temperatures from the liquid to the glass state. It can be seen that at high temperatures, the MSD of the ion centers-of-mass exhibits the characteristic diffusive behavior of simple liquids. With decreasing temperature, the mobility of the ions is dramatically reduced, and the glass state can be observed below 300 K. At very short times ($t < 1.0$ ps), the MSD shows a quadratic dependence in time and a weak behavior with temperature. At longer times, there is a transition to the characteristic diffusive regime of the liquid, which is strongly temperature dependent. Between these two limits, an intermediate subdiffusive regime appears,¹⁷ becoming increasingly extended with decreasing temperature. This intermediate region indicates that the ions are vibrating within “cages” of neighbors that are stable within time scales of several hundred picoseconds.

To observe the liquid-glass transition region more clearly, the MSD at four observation times is plotted as a function of temperature and shown in Figure 7. For the smallest time (1.0 ps), the MSD follows the expected behavior (dashed linear line) up to room temperatures. Below 250 K, the global motion of the ions is arrested, and at each temperature, the MSD mainly exhibits small fluctuations (< 0.1 Å²) at the observation times. The deviations from the cage regime are observed at larger times when the temperature is high enough. Overall, the departure from linear behavior in the MSD occurs at around 250–275 K, which is qualitatively identified as the glass-transition region, close to the experimentally reported melting/glass-transition temperature, 273 K.⁵⁴ The same has been found in other computer simulations and suggests a relationship between the short-time dynamics and the phenomena observed on much longer time scales.⁵⁵ The departure from linear behavior with increasing temperature can be viewed as a precursor of the glass-liquid transition,^{55,56} which takes place when anharmonicities are large enough to overcome the restoring caging forces that form the mechanically stable arrangement corresponding to a particular minimum of the configuration space, so that the system starts to explore other minima of the full configuration space.⁵⁷ Here, it should be stressed that the identification of the glass-transition region via MD simulation^{49–51} depends on the cooling rate of the simulated annealing, and therefore, the glass-transition region may not be well-defined.

The reorientational time correlation function, $P_2(t)$, is given by

$$P_2(t) = \langle 3/2 [\mathbf{u}_i(t) \cdot \mathbf{u}_i(0)]^2 - 1/2 \rangle \quad (6)$$

where $\mathbf{u}_i(t)$ is a normal unit vector on the plane of NO₃⁻ or the triazolium ring of cation. Figure 8a and b shows the reorientational correlation functions for the same temperatures as those in Figure 6. It can be seen that the temperature-dependent orientational behavior of the cation is the same as its translational behavior. In contrast, the orientational behavior of the anion does not show any sign of dynamical arrest. Such a decoupling between translational and orientational degrees of freedom is usually connected with activated translational or orientational hopping processes, which can be studied by Van Hove self-correlation functions described later.

Structural relaxation can be studied from the self-part of the intermediate scattering function, $F_s(k, t)$

$$F_s(k, t) = \langle \exp\{i\mathbf{k} \cdot [\mathbf{r}_i(t) - \mathbf{r}_i(0)]\} \rangle \quad (7)$$

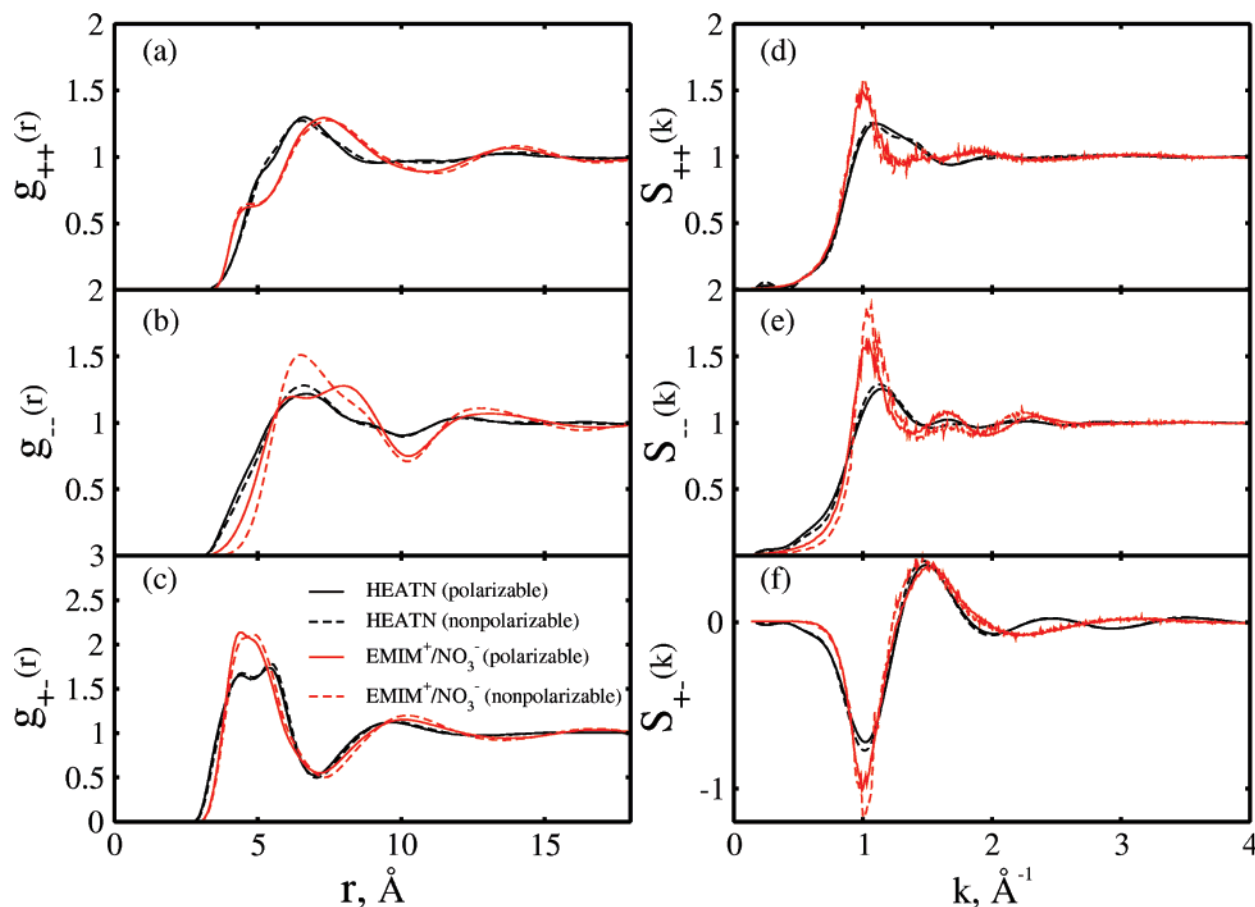


Figure 4. The center-of-mass partial radial distribution functions for (a) cation–cation, (b) anion–anion, and (c) cation–anion and the static structure factors for (d) cation–cation, (e) anion–anion, and (f) cation–anion. The solid lines are for the polarizable model, and the dashed lines are for the nonpolarizable model.

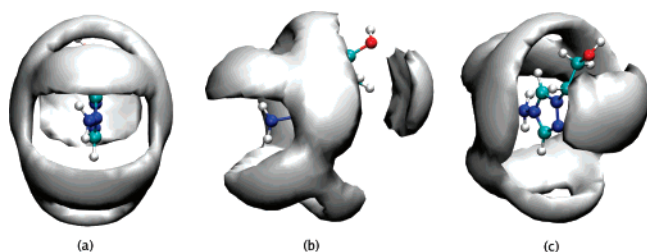


Figure 5. Three-dimensional configurational probability distribution of NO₃⁻ around the cation, viewed in three different directions along the cation. The isosurfaces represent regions with an anion density 3 times that of the bulk density.

where $k = |\mathbf{k}|$ are the wave vectors of the same modulus. The calculation of $F_s(k, t)$ was performed for a set of discrete k values chosen of the form $(2\pi/L)(n_1, n_2, n_3)$, with $n_{1,2,3}$ an integer. To ensure good statistics of the calculated $F_s(k, t)$, all of the combinations of (n_1, n_2, n_3) that lead to the same value of k were used. Figure 8c and d shows the temperature-dependent structural relaxation of ions at $k = 1.032 \text{ \AA}^{-1}$ (around the first minimum of the cation–anion partial static structure factor). It can be observed that the structural relaxations display a two-step decay observed in glass-forming liquids, where an initial short-time decay is followed by a plateau at intermediate times and then a slow decay (α relaxation), which is stretched in time. The latter appears to be temperature sensitive and slows down significantly when approaching T_g . It also can be noticed that there is no appreciable boson peak⁴⁸ in $F_s(\mathbf{k}, t)$ at a glass-transition temperature at ~ 1.0 ps, that is, shortly after the

microscopic dynamics regime and before the correlator shows its plateau. This feature suggests that HEATN may be a fragile glass former at room temperature.

Equation 7 is the spatial Fourier transform of the Van Hove self-correlation function, which is given by

$$G_s(\mathbf{r}, t) = \frac{1}{N} \left\langle \sum_{i=1}^N \delta(\mathbf{r}_i^c(t) - \mathbf{r}_i^c(0) - \mathbf{r}) \right\rangle \quad (8)$$

The Van Hove self-correlation function measures the probability that the center-of-mass of a molecule is at position $\mathbf{r}_i^c(t)$ at time t given that it was at the origin, $\mathbf{r}_i^c(0)$, at time 0. In Figure 9, this function is plotted for the ion centers-of-mass at three temperatures. At 450 K (panel a), the curve corresponding to several times t has a single peak whose maximum moves to larger distances with increasing time, indicative of diffusive motion. Such peak shifts are nearly arrested at 275 K, that is, about the temperature where the MSD only shows a very weak sign of mass diffusion. Finally, at 175 K, there is no longer any trace of diffusive motion after the initial vibrational relaxation; therefore, the system is completely arrested. On the other hand, activated hopping processes are usually detected by Van Hove correlation functions. In hopping processes occurring at low temperatures, a secondary peak in $G_s(\mathbf{r}, t)$ is observed at large distances at long times. In Figure 9, no secondary peak can be observed, and therefore, the ion hopping process is not evident in the supercooled HEATN system.

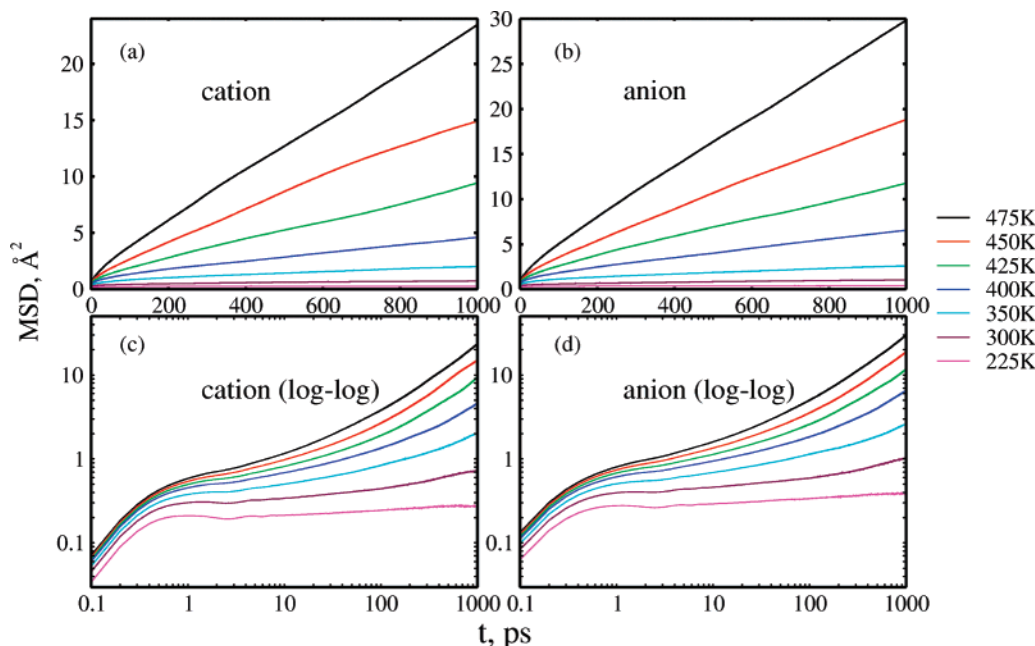


Figure 6. Temperature-dependent mean-squared displacement (MSD). Panels (a) and (c) show the MSDs of the cation; panels (b) and (d) show the MSDs of the anion. The logarithmic time scale was employed in panels (c) and (d) to highlight the intermediate subdiffusive regimes.

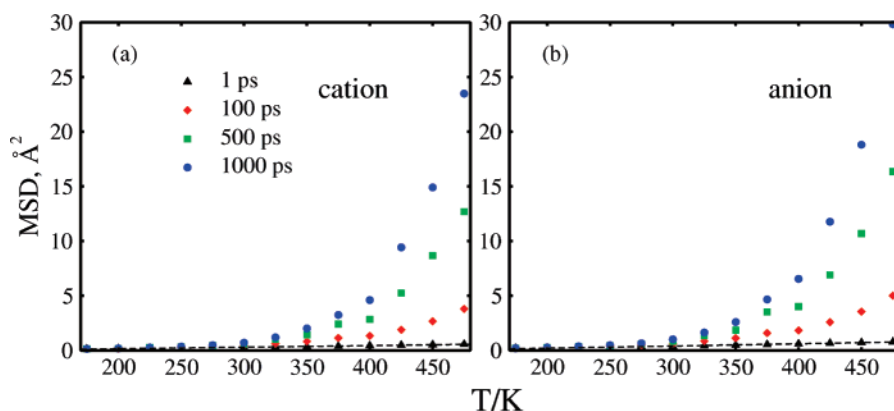


Figure 7. Temperature dependence of MSD at four different observation times. Note that the departure from linearity (black dashed line) occurs around 250–270 K.

An orientational analogue to $G_s(\mathbf{r}, t)$ can be also defined, that is

$$G_{or}(\theta, t) = \frac{1}{N} \left\langle \sum_{i=1}^N \delta(\theta + \theta_i(0) - \theta_i(t)) \right\rangle \quad (9)$$

where $\theta_i(t)$ is the angle made by a unit vector on the C_3 axis of a given NO_3^- anion or a unit normal vector on the triazolium ring of a given cation at time t to its value $\theta_i(0)$ at time 0. Figure 10 shows $G_{or}(\theta, t)$ at the same temperatures as that in Figure 9. Reorientational hopping processes can be clearly seen among the anions, while only reorientational arrest happens to the cations. This can be explained by the symmetric planar structure of NO_3^- , that is, both sides of the anion plane are favored in the cation–anion interactions. The reorientational hopping process of the anion also explains the decoupling between its translational and reorientational dynamics. In contrast, due to the relatively large size and asymmetric geometrical structure along the triazolium ring, the reorientational hopping process of the cation is forbidden.

C. Transport Properties. Figure 11 shows the MSD of the cation and anion for both the polarizable and nonpolarizable models at 400 K, up to 1 ns. Remarkably, the slope of the MSD of the polarizable model is more than twice as large as that of the nonpolarizable model by 1 ns, similar to the behavior seen in $\text{EMIM}^+/\text{NO}_3^-$.⁴⁰ A linear fit to the MSD and using the Einstein relation, $\langle \Delta r(t)^2 \rangle = 6Dt$, gives the diffusion constants 1.73×10^{-11} and $2.63 \times 10^{-11} \text{ m}^2/\text{s}$ for the cation and anion, respectively, for the polarizable model and 0.74×10^{-11} and $0.80 \times 10^{-11} \text{ m}^2/\text{s}$ for the cation and anion, respectively, for the nonpolarizable model. It should be stressed that the self-diffusion values for HEATN are nearly 1 order of magnitude smaller than those of $\text{EMIM}^+/\text{NO}_3^-$.⁴⁰ This feature demonstrates that the amino and the hydroxyl groups of HEATN dramatically decrease the diffusive dynamics due to their strong electrostatic attraction to the anions. It should also be noted that the many-body polarizability effectively smears the “electrostatic cage” effect in ILs, and therefore, the diffusive regime appears significantly earlier than it does with the nonpolarizable model.⁴⁰ For the latter, it is known that a MD simulation with at least

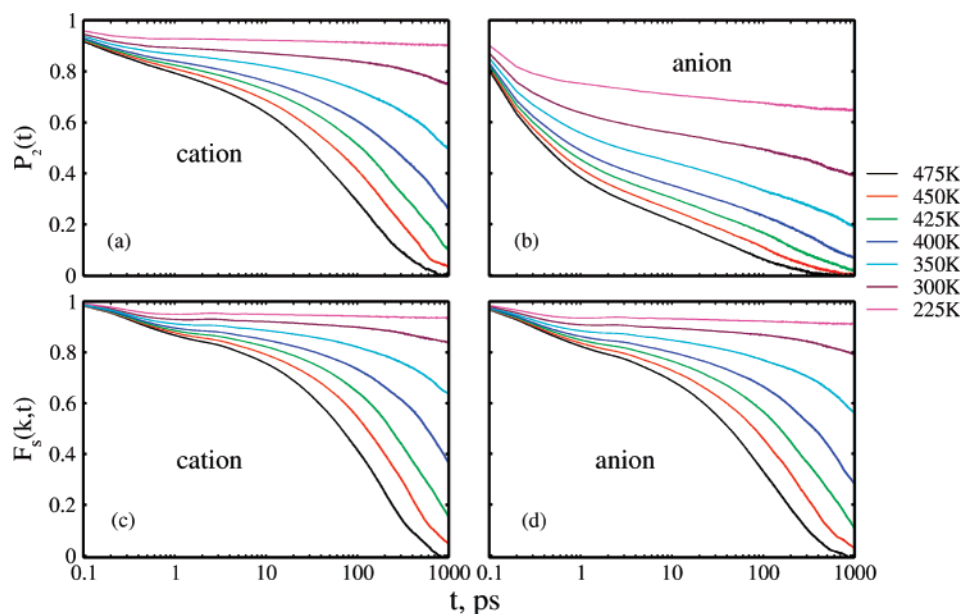


Figure 8. Temperature dependence of reorientational and structural relaxations. Panels (a) and (b) show reorientational relaxations for the cation and anion, respectively; panels (c) and (d) show structural relaxations for the cation and anion, respectively. Note that the self-part of the intermediate scattering functions of both the cation and anion have a vanishing “boson peak” at the glass-transition region. The faster reorientational relaxation of the anion than the cation is observed.

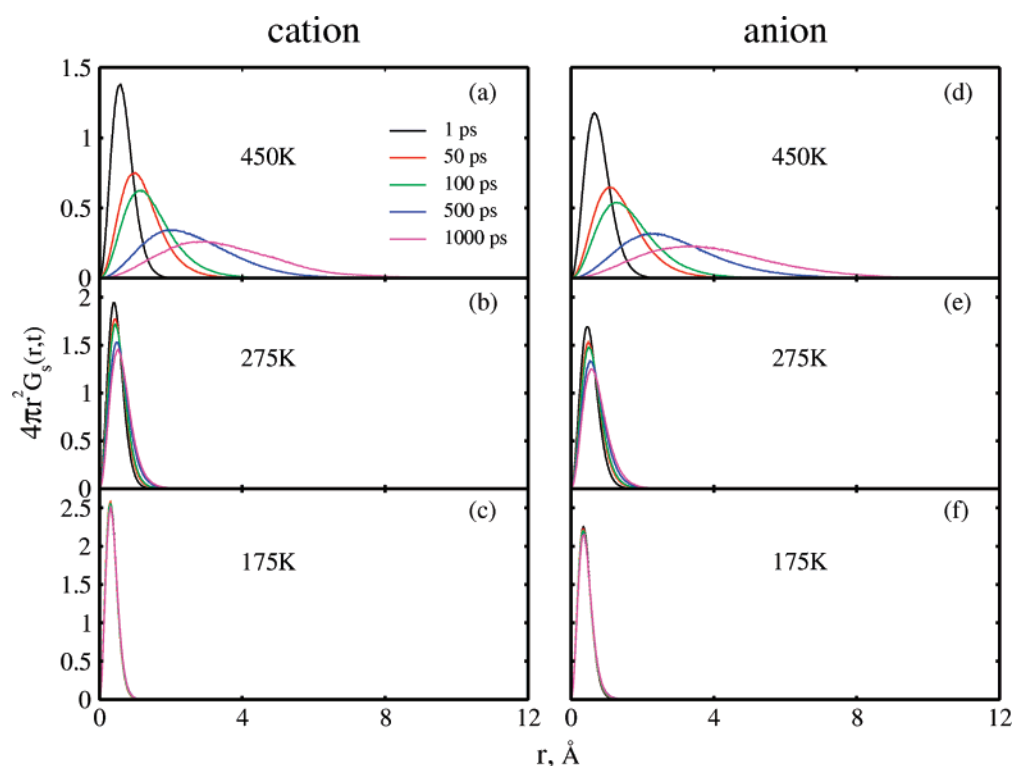


Figure 9. The translational Van Hove self-correlation functions at three selected temperatures for both the cation ((a), (b), and (c)) and anion ((d), (e), and (f)). The arrest of translational motion as the temperature goes below the glass-transition point can be observed.

tens of nanoseconds^{17,52} is necessary to accurately compute the transport properties of ILs.

For energetic ILs, the shear viscosity is related to the fuel source viability. The simplest method for the evaluation of the shear viscosity η is through the standard Green–Kubo relation⁵⁸

$$\eta = \frac{1}{VK_B T} \int_0^\infty dt \langle \sigma^{xy}(0) \sigma^{xy}(t) \rangle \quad (10)$$

where $\sigma^{xy}(t)$ is one of the off-diagonal components of the stress tensor. This method, due to the slow convergence of the correlation function with time, is difficult to apply to viscous systems such as ionic liquids. An alternative route to the evaluation of η involves the calculation of the wave-vector-dependent transverse-current autocorrelation function (TCAC)⁵⁸

$$C_t(k, t) = \frac{\langle \mathbf{J}_t(\mathbf{k}, t) \cdot \mathbf{J}_t(-\mathbf{k}, 0) \rangle}{\langle \mathbf{J}_t(\mathbf{k}, 0) \cdot \mathbf{J}_t(-\mathbf{k}, 0) \rangle} \quad (11)$$

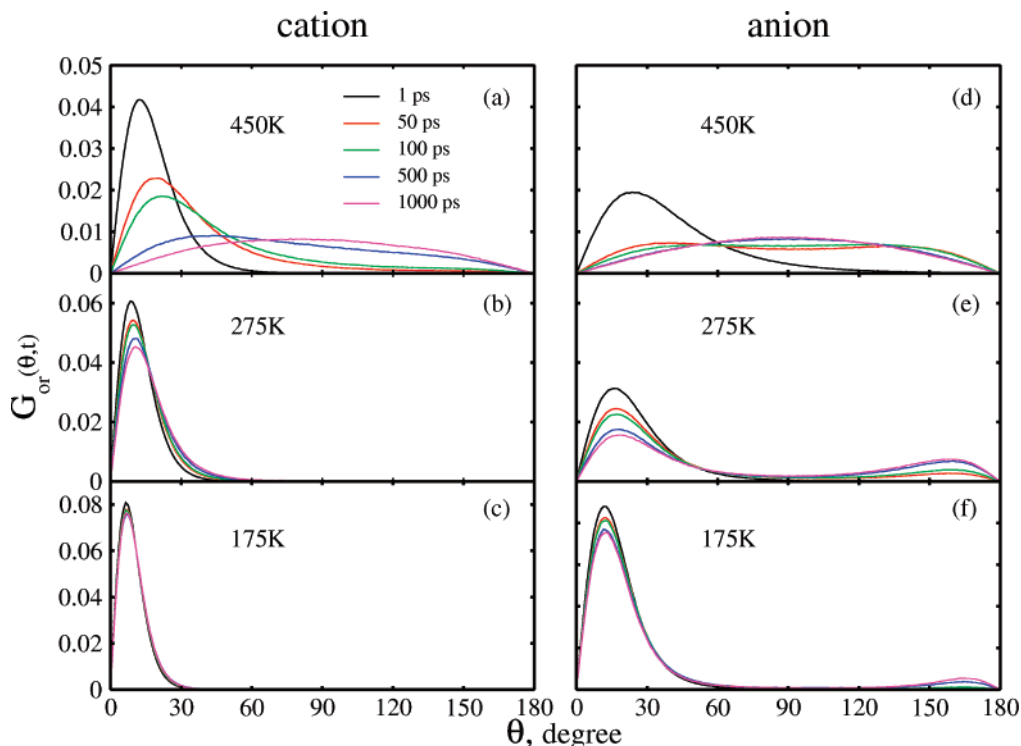


Figure 10. The orientational Van Hove self-correlation functions at the same temperatures as those in Figure 9 for both the cation ((a), (b), and (c)) and anion ((d), (e), and (f)). Note that the cation shows the same arrest of the orientational motion as that of the translational motion, while the anion shows distinct orientational activated hopping.

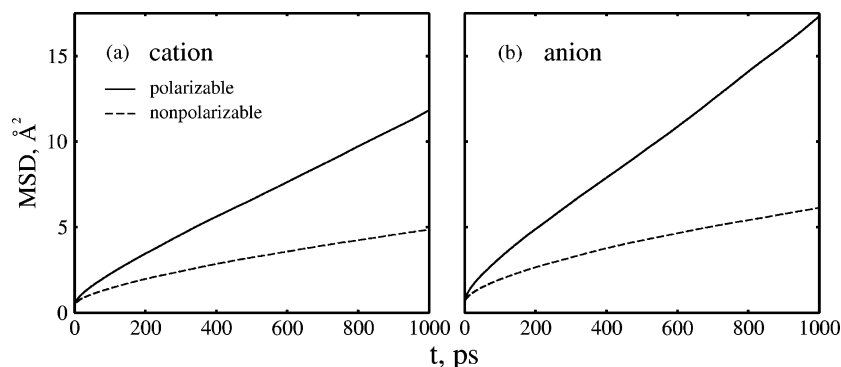


Figure 11. MSDs of the cation (a) and anion (b) for the polarizable model (solid lines) and nonpolarizable model (dashed lines) at 400 K.

where $\mathbf{J}_t(\mathbf{k}, t)$ is the total transverse current operator. For a binary liquid, $\mathbf{J}_t(\mathbf{k}, t)$ is given by

$$\mathbf{J}_t(\mathbf{k}, t) = \frac{1}{\sqrt{N}} \sum_{i=1}^N \mathbf{k} \times m_i \mathbf{v}_i(t) \exp[i\mathbf{k} \cdot \mathbf{r}_i(t)] \quad (12)$$

where m_i , \mathbf{v}_i , and $\mathbf{r}_i(t)$ are the mass, center-of-mass velocity, and position of the i th ion, respectively.

As is well-known in the hydrodynamic ($k \rightarrow 0$) limit, $C_t(k, t)$ turns out to be

$$C_t(k \rightarrow 0, t) = \exp\left(-k^2 \frac{\eta}{\rho} |t|\right) \quad (13)$$

where ρ is the mass density. In the Mori–Zwanzig projection formalism, one can define a generalized viscosity proportional to the memory function of $C_t(k, t)$ such that the Laplace transform of $C_t(k, t)$, $M_t(k, z)$ reads as

$$M_t(k, z) = \frac{1}{z + (k^2/\rho)\eta(k, z)} \quad (14)$$

From eq 15, one readily derives in the $z = 0$ limit

$$\eta(k, z = 0) = \frac{\rho}{k^2} \frac{1}{M_t(k, z = 0)} \quad (15)$$

Thus, a wave-vector-dependent generalized viscosity can be directly derived from computer simulation results of a more easily obtainable quantity. The extrapolation to $k = 0$ for eq 15 gives the hydrodynamic value of this generalized transport coefficient, namely, the usual shear viscosity.

Figure 12 shows the transverse current correlation function, $C_t(k, t)$, at four selected wave vectors for the polarizable and nonpolarizable models. The value $k = 0.172 \text{ \AA}^{-1}$ is the smallest wave vector allowed by the periodic simulation cell. Comparing the $C_t(k, t)$ of the same wave vectors for both models, especially at lower k , it can be seen that the negative minimum in $C_t(k, t)$ of the polarizable model is shallower and occurs at a later time than that in the nonpolarizable model, which is an indication of the lower viscosity in the polarizable model.

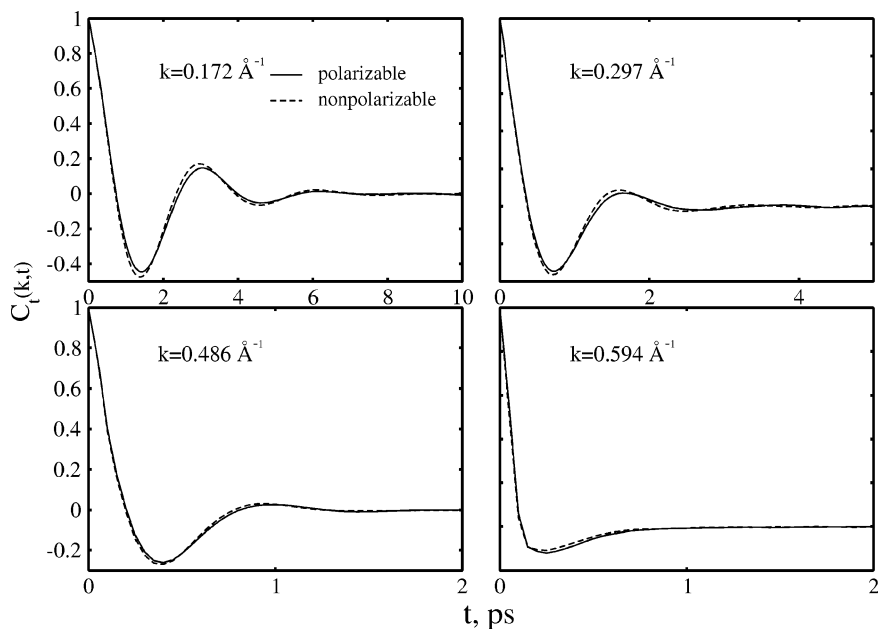


Figure 12. Four selected normalized transverse current correlation functions $C_t(k,t)$ of both the polarizable model (solid line) and nonpolarizable model (dashed line).

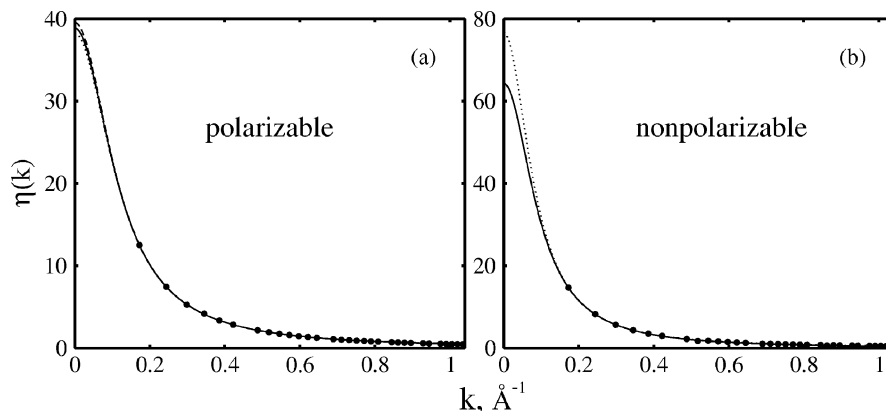


Figure 13. The wave-vector-dependent shear viscosity $\eta(k)$ calculated by eq 16 at different values of k . (a) Fitted $\eta(k)$ of the polarizable model; (b) fitted $\eta(k)$ of the nonpolarizable model. The solid lines represent the ultimate converged fitting.

In principle, an extrapolation can be obtained by fitting the simulation data with an expression

$$\eta(k) = \frac{\eta}{1 + \sum_{m=1} a_m k^{2m}} \quad (16)$$

which can be obtained from the inversion symmetry of $\eta(k)$ in k space.⁵⁸ At not too large k vectors, only a limited number of terms are necessary. For example, for a dense hard-sphere system, only the $m = 1$ term is necessary, and such a simple fitting procedure has been widely used for liquids of low viscosity.^{59–61} For ionic liquids, the higher viscosity and limited size of the MD simulation often requires higher-order terms to be included to ensure a converged fit. Figure 13 shows the extrapolation to zero k by the simulated data. There, the largest k value used corresponds to the characteristic length scale of the microscopic structure (Figure 4). As the number of terms increases, it can be seen that the fitted viscosity goes to a converged value, which is 38.21 cP for the polarizable model and 64.25 cP for the nonpolarizable model. The electronic polarizability thus has a large effect on the IL viscosity, as also found in our previous study of the EMIM⁺/NO₃[−] IL.⁴⁰

Since there are no experimental data for the viscosity of HEATN at present, an estimation of whether the viscosity of the simulated system is reasonable has to be obtained by comparing the obtained diffusion and viscosity data for EMIM⁺/NO₃[−] and HEATN, which have a similar molecular size and geometrical conformation. At 400 K, both IL systems are far from the glass-transition region; thus, the Stokes–Einstein (S–E) relation, $D\eta \propto r/kT$, where r denotes the molecular radius, may provide a reasonable estimate. The simulated viscosity of EMIM⁺/NO₃[−] is 4.76 (experimental value, 4.42 cP) and 6.84 cP for the polarizable and nonpolarizable models, respectively.⁴⁰ After substituting diffusion and viscosity data of the ILs into the S–E relation, it can be seen that the relation is approximately obeyed, and therefore, the calculated viscosity for HEATN is reasonable. It is important to note that Hu and Margulis⁶² have systematically studied the response of an ionic liquid to external perturbations and the calculation of shear viscosity. In their work, the periodic perturbation method was shown to be more robust to estimate the shear viscosity, compared to the present TCAC-based method. The implementation of the periodic perturbation method with the polarizable model, as well as MD simulations with significantly larger simulation cells, will be a focus of future research.

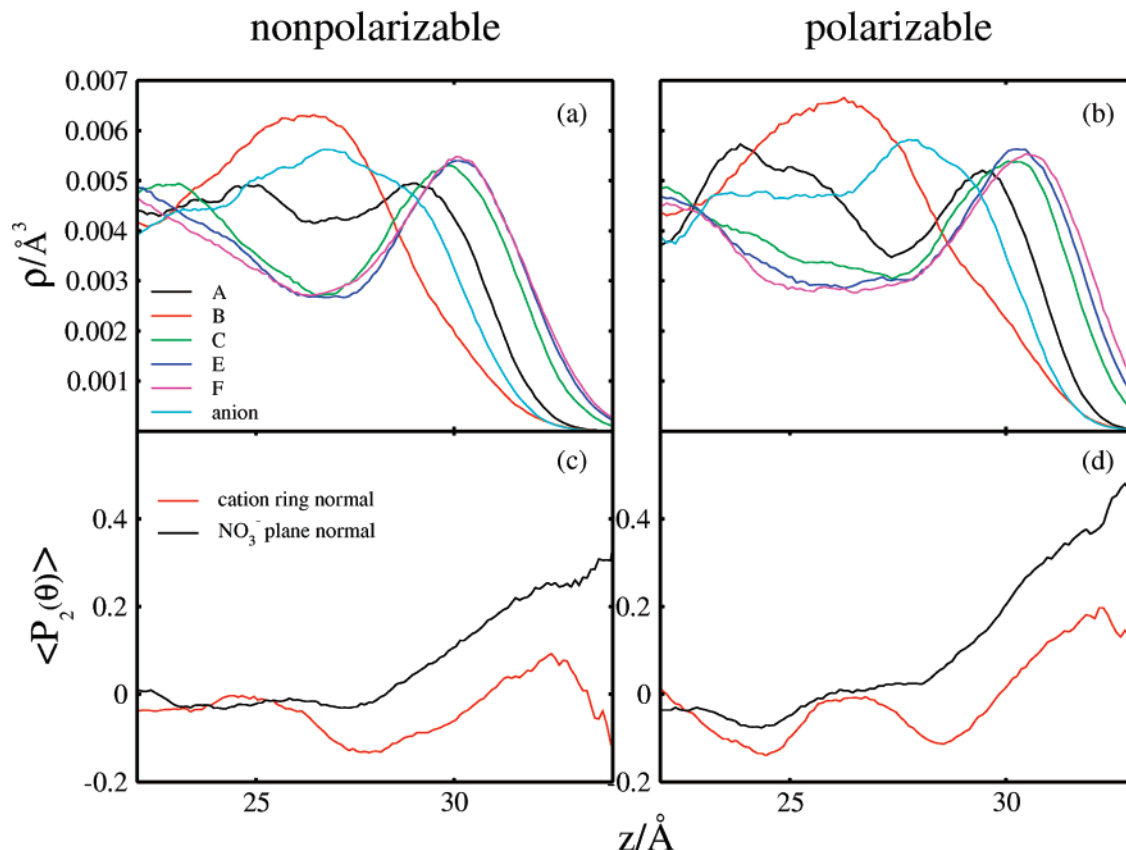


Figure 14. Number density profile and orientational ordering parameter of cations and anions at the liquid/vacuum interface for both the nonpolarizable model ((a) and (c)) and the polarizable model ((b) and (d)). In the top two plots, the vanishing surface layering due to the existence of a hydroxyl group can be seen. In the bottom two plots, θ is defined by the angle between the direction vectors and the surface normal: red for the normal vector of the cation ring and black for the plane-normal vector of NO_3^- . The sites B, A, C, E, and F represent the center-of-mass for the amino group, triazolium ring, methylene group, methylene group, and hydroxyl group successively along the cation. Site D denotes the center-of-mass for nitrate. In panels (a) and (b), no error bar is larger than $\pm 1.93 \times 10^{-4}$, and in panels (c) and (d), no error bar is larger than $\pm 1.57 \times 10^{-2}$.

D. Structural Properties of the Liquid/Vacuum Interface. Panels a and b of Figure 14 show the surface-normal density profiles (DPFs) at the liquid/vacuum interface for the nonpolarizable and polarizable models, respectively. Panels c and d show the corresponding interfacial orientational ordering parameter and are defined in the same way as eq 6 for both the polarizable model and nonpolarizable model. It can be seen that the two models give similar results. As observed in $\text{EMIM}^+/\text{NO}_3^-$,⁶³ there is an obvious density enhancement at the interface, indicating a denser ion packing behavior in this region. In contrast to the interfacial structure of $\text{EMIM}^+/\text{NO}_3^-$, however, there is no obvious surface layering controlled by the alkyl chain; the surface-normal DPFs of the hydroxyl group (site F) and the terminal methylene groups (sites C and E) almost overlap at the interface, despite the fact that the amino group, triazolium ring, and the intermediate methylene group have a considerable orientational tendency due to the formation of rigid-like structures. Correspondingly, the cation shows a weak interfacial orientational preference. Such a minimal surface layering and orientational tendency can be explained by the strong ion–ion hydrogen-bonding interactions. In the imidazolium-based ILs, the nonpolar alkyl tail causes a two-dimensional polar/nonpolar phase segregation so that a clear surface layering can be observed. However, in HEATN, the introduction of the hydroxyl group on the terminal end of the nonpolar alkyl chain and the amino group on the triazolium ring causes both terminals of the cation to tend to approach the anion, breaking up the successive arrangement of functional groups and ring orientation seen in imidazolium-based ILs. However, the above mechanism is not applicable to the anion.

Due to the close competition between anion–amino and anion–hydroxyl interactions along the two opposite directions along the cation, the anion retains a strong orientational tendency, as illustrated in panels c and d.

According to the Langmuir principle,⁶⁴ the measured surface tension of a liquid should correspond to the part of the molecule that is actually present at the interface. For imidazolium-based ILs, due to the essence of van der Waals interactions, the protruding nonpolar methylene groups result in a relatively lower surface free energy and small surface tension, while for HEATN, the strong polar hydroxyl group at the outermost region causes a much higher surface tension. The surface tension was calculated with both the polarizable and nonpolarizable models, giving values of 94 ± 3 and 68 ± 3 mN/m, respectively. These values are to be compared to 58 and 83 mN/m, respectively, for $\text{EMIM}^+/\text{NO}_3^-$ at 400 K.⁶³ Interestingly, for the two ILs, the electronic polarizability has an opposite effect on the surface tension. This may be a result of the qualitative difference between the interfacial structure of these two ILs.

IV. Concluding Remarks

In this study, molecular dynamics simulations of HEATN have estimated a glass-transition temperature region at around 250–275 K, in agreement with the experimentally reported melting/glass-transition point.⁵⁴ The vanishing boson peaks observed in the structural relaxation suggest that HEATN may be a fragile glass former. The coupling of translational and orientational dynamics of the cation from the liquid to glass state was observed, while the anion showed a decoupling of

the corresponding dynamical behavior due to its orientational hopping. A significant hydrogen bond network was observed and is responsible for the poor ion packing efficiency, which is an indication of a low melting/glass-transition point. The ionic liquid substituted by a hydroxyl and amino group not only shows poorer packing and a lower glass-transition point but also has strongly effected transport properties. Compared to similar-sized imidazolium-based ILs, HEATN's self-diffusion coefficient is nearly 1 order of magnitude smaller, and the shear viscosity is almost 1 order of magnitude higher due to the strong electrostatic attraction caused by the amino and hydroxyl groups. The hydroxyl group also dramatically affects the interfacial structural properties. Its strong polarity breaks the surface layering and thus results in a higher surface tension than that of EMIM⁺/NO₃⁻. Our future work will continue to explore these relationships between molecular structure and useful physical properties for ILs.

Acknowledgment. This research was supported by the Air Force Office of Scientific Research. The authors thank Dr. Qiang Shi, Dr. Gary Ayton, and Dr. Satoru Iuchi for valuable discussions. The computations in this work were carried out through a challenge grant from the Department of Defense High Performance Computing Modernization Office.

Supporting Information Available: The generalized amber force field (GAFF) parameters for HEATN. This material is available free of charge via the Internet at <http://pubs.acs.org>.

References and Notes

- (1) Rogers, R. D.; Seddon, K. R. *Science* **2003**, *302*, 792.
- (2) Wasserscheid, P.; Keim, W. *Angew. Chem., Int. Ed.* **2000**, *39*, 3772.
- (3) Welton, T. *Chem. Rev.* **1999**, *99*, 2071.
- (4) Gordon, C. M.; Holbrey, J. D.; Kennedy, A. R.; Seddon, K. R. *J. Mater. Chem.* **1998**, *8*, 2627.
- (5) Hagiwara, R.; Ito, Y. *J. Fluorine Chem.* **2000**, *105*, 221.
- (6) Holbrey, J. D.; Seddon, K. R. *J. Chem. Soc., Dalton Trans.* **1999**, 2133.
- (7) Zhao, Y.; Vandernoot, T. *J. Electrochim. Acta* **1997**, *42*, 3.
- (8) MacFarlane, D. R.; Huang, J.; Forsyth, M. *Nature (London)* **1999**, *402*, 792.
- (9) Garcia, B.; Lavalley, S.; Perron, G.; Michot, C.; Armand, M. *Electrochim. Acta* **2004**, *49*, 4583.
- (10) Carlin, R. T.; Fuller, J. *Chem. Commun.* **1997**, 1345.
- (11) Noda, A.; Watanabe, M. *Electrochim. Acta* **2000**, *45*, 1265.
- (12) Yoshizawa, M.; Hirao, M.; Ito-akita, K.; Ohno, H. *J. Mater. Chem.* **2001**, *11*, 1057.
- (13) Snedden, P.; Cooper, A. I.; Scott, K.; Winterton, N. *Macromolecules* **2003**, *36*, 4549.
- (14) Fukushima, T.; Kosaka, A.; Ishimura, Y.; Yamamoto, T.; Takigawa, T.; Ishii, N.; Aida, T. *Science* **2003**, *300*, 2072.
- (15) Lee, C. K.; Huang, H. W.; Lin, I. J. B. *Chem. Commun.* **2000**, 1911.
- (16) Lee, K. M.; Lee, C. K.; Lin, I. J. B. *Chem. Commun.* **1997**, 899.
- (17) Del Popolo, M. G.; Voth, G. A. *J. Phys. Chem. B* **2004**, *108*, 1744.
- (18) Margulis, C. J. *Mol. Phys.* **2004**, *102*, 829.
- (19) Urahata, S. M.; Ribeiro, M. C. C. *J. Chem. Phys.* **2004**, *120*, 1855.
- (20) Wang, Y.; Voth, G. A. *J. Am. Chem. Soc.* **2005**, *127*, 12192.
- (21) Canongia Lopes, J. N.; Padua, A. A. H. *J. Phys. Chem. B* **2006**, *110*, 3330.
- (22) Jiang, W.; Wang, Y.; Voth, G. A. *J. Phys. Chem. B* **2007**, *111*, 4812.
- (23) Wilkes, J. S. In *Green Industrial Applications of Ionic Liquids*; Rogers, R. D.; Seddon, K. R.; Volkov, S., Eds.; Springer: New York, 2002.
- (24) Carpio, R. A.; King, L. A.; Kibler, F. C.; Fannin, A. A. *J. Electrochem. Soc.* **1979**, *126*, 1650.
- (25) Wilkes, J. S.; Levitsky, J. A.; Wilson, R. A.; Hussey, C. L. *Inorg. Chem.* **1982**, *21*, 1263.
- (26) Wilkes, J. S.; Zaworotko, M. J. *J. Chem. Soc., Chem. Commun.* **1992**, 965.
- (27) Seddon, K. R.; Stark, A.; Torres, M.-J. *Clean Solvents: Alternative Media for Chemical Reactions and Processing*; Abraham, M., Moens, L., Eds.; ACS Symposium Series 819; American Chemical Society: Washington, DC, 2002; pp 34–39.
- (28) Drake, G.; Hawkins, T.; Brand, A.; Hall, L.; McKay, M. *Propellants, Explos., Pyrotech.* **2003**, *28*, 174.
- (29) Drake, G. W.; Hawkins, T. W.; Boatz, J.; Leslie, H.; Vij, A. *Propellants, Explos., Pyrotech.* **2005**, *30*, 156.
- (30) Verma, R. D.; Shreeve, J. M.; Singh, R. P.; Meshri, D. T. *Angew. Chem., Int. Ed.* **2006**, *45*, 3584.
- (31) Hong, X.; Shreeve, J. M. *Adv. Mater.* **2005**, *17*, 2142.
- (32) Xue, H.; Artritt, S. W.; Twamley, B.; Shreeve, J. M. *Inorg. Chem.* **2004**, *43*, 7972.
- (33) Schmidt, M. W.; Gordon, M. S.; Boatz, J. A. *J. Phys. Chem. A* **2005**, *109*, 7285.
- (34) Zorn, D. D.; Boatz, J. A.; Gordon, M. S. *J. Phys. Chem. B* **2006**, *110*, 11110.
- (35) Gutowski, K. E.; Holbrey, J. D.; Rogers, R. D.; Dixon, D. A. *J. Phys. Chem. B* **2005**, *109*, 23196.
- (36) Alavi, S.; Thompson, D. L. *J. Phys. Chem. B* **2005**, *109*, 18127.
- (37) Cadena, C.; Maginn, E. J. *J. Phys. Chem. B* **2006**, *110*, 18026.
- (38) Stern, H. A.; Kaminski, G. A.; Banks, J. L.; Zhou, R.; Berne, B. J.; Friesner, R. A. *J. Phys. Chem. B* **1999**, *103*, 4730.
- (39) Stern, H. A.; Rittner, F.; Berne, B. J.; Friesner, R. A. *J. Chem. Phys.* **2001**, *115*, 2237.
- (40) Yan, T.; Burnham, C. J.; Del Popolo, M. G.; Voth, G. A. *J. Phys. Chem. B* **2004**, *108*, 11877.
- (41) Car, R.; Parrinello, M. *Phys. Rev. Lett.* **1985**, *55*, 2471.
- (42) Cornell, W. D.; Cieplak, P.; Bayly, C. I.; Gould, I. R.; Merz, K. M.; Ferguson, D. M.; Spellmeyer, D. C.; Fox, T.; Caldwell, J. W.; Kollman, P. A. *J. Am. Chem. Soc.* **1995**, *117*, 5179.
- (43) Wang, J.; Wolf, R. M.; Caldwell, J. W.; Kollman, P. A.; Case, D. A. *J. Comput. Chem.* **2004**, *25*, 1157.
- (44) Bayly, C. I.; Cieplak, P.; Cornell, W. D.; Kollman, P. A. *J. Phys. Chem.* **1993**, *97*, 10269.
- (45) Frisch, M. J.; Trucks, G. W.; Schlegel, H. B.; Scuseria, G. E.; Robb, M. A.; Cheeseman, J. R.; Montgomery, J. A., Jr.; Vreven, T.; Kudin, K. N.; Burant, J. C.; Millam, J. M.; Iyengar, S. S.; Tomasi, J.; Barone, V.; Mennucci, B.; Cossi, M.; Scalmani, G.; Rega, N.; Petersson, G. A.; Nakatsuji, H.; Hada, M.; Ehara, M.; Toyota, K.; Fukuda, R.; Hasegawa, J.; Ishida, M.; Nakajima, T.; Honda, Y.; Kitao, O.; Nakai, H.; Klene, M.; Li, X.; Knox, J. E.; Hratchian, H. P.; Cross, J. B.; Bakken, V.; Adamo, C.; Jaramillo, J.; Gomperts, R.; Stratmann, R. E.; Yazyev, O.; Austin, A. J.; Cammi, R.; Pomelli, C.; Ochterski, J. W.; Ayala, P. Y.; Morokuma, K.; Voth, G. A.; Salvador, P.; Dannenberg, J. J.; Zakrzewski, V. G.; Dapprich, S.; Daniels, A. D.; Strain, M. C.; Farkas, O.; Malick, D. K.; Rabuck, A. D.; Raghavachari, K.; Foresman, J. B.; Ortiz, J. V.; Cui, Q.; Baboul, A. G.; Clifford, S.; Cioslowski, J.; Stefanov, B. B.; Liu, G.; Liashenko, A.; Piskorz, P.; Komaromi, I.; Martin, R. L.; Fox, D. J.; Keith, T.; Al-Laham, M. A.; Peng, C. Y.; Nanayakkara, A.; Challacombe, M.; Gill, P. M. W.; Johnson, B.; Chen, W.; Wong, M. W.; Gonzalez, C.; Pople, J. A. *Gaussian 03*; Gaussian, Inc.: Wallingford, CT, 2004.
- (46) Thole, B. T. *Chem. Phys.* **1981**, *59*, 341.
- (47) Trohalaki, S.; Pachter, R.; Drake, G. W.; Hawkins, T. *Energy Fuels* **2005**, *19*, 279.
- (48) Walter, K. J. *Phys.: Condens. Matter* **1999**, *11*, R85.
- (49) Gonzalez, M. A.; Enciso, E.; Bermejo, F. J.; Bee, M. *Phys. Rev. B* **2000**, *61*, 6654.
- (50) Tsige, M.; Taylor, P. L. *Phys. Rev. E* **2002**, *65*, 021805.
- (51) Ribeiro, M. C. C. *J. Phys. Chem. B* **2003**, *107*, 9520.
- (52) Schroder, C.; Rudas, T.; Steinhäuser, O. *J. Chem. Phys.* **2006**, *125*, 244506.
- (53) Hu, Z.; Margulis, C. J. *Proc. Natl. Acad. Sci. U.S.A.* **2006**, *103*, 831.
- (54) Hawkins, T. W. Unpublished.
- (55) Angell, C. A. *Science* **1995**, *267*, 1924.
- (56) Roe, R. J. *J. Chem. Phys.* **1994**, *100*, 1610.
- (57) Stillinger, F. H. *Science* **1995**, *267*, 1935.
- (58) Balucani, U.; Zoppi, M. *Dynamics of the Liquid State*; Clarendon: Oxford, U.K., 1994.
- (59) Alley, W. E.; Alder, B. *Phys. Rev. A* **1983**, *27*, 3158.
- (60) Palmer, B. J. *Phys. Rev. E* **1994**, *49*, 359.
- (61) Balucani, U.; Brodtholt, J. P.; Jedlovsky, P.; Vallauri, R. *Phys. Rev. E* **2000**, *62*, 2971.
- (62) Hu, Z.; Margulis, C. J. *J. Phys. Chem. B* **2007**, *111*, 4705.
- (63) Yan, T.; Li, S.; Jiang, W.; Gao, X.; Xiang, B.; Voth, G. A. *J. Phys. Chem. B* **2006**, *110*, 1800.
- (64) Langmuir, I. *Colloid Symp. Monogr.* **1925**, *48*.